Fe-Loaded Two-Dimensional Nitrogen-Doped Carbon for Electromagnetic Wave Absorption

Xi Wen[1†], Yang Qin[2†], Yu Hao[1], Geng Chang[1], Kai Huang[3], Ming Lei[2], Xiaojun Shen[1], Yong He[1], Xuchao Pan[1*], and Yufeng Wu[3*]

[1]*Ministerial Key Laboratory of ZNDY, Nanjing University of Science & Technology, Nanjing 210094, China*
[2]*State Key Laboratory of Information Photonics and Optical Communications, School of Integrated Circuits, Beijing University of Posts and Telecommunications, Beijing 100876, China*
[3]*State Key Laboratory of Information Photonics and Optical Communications, School of Science, Beijing University of Posts and Telecommunications, Beijing 100876, China*

(Received 21 September 2024; accepted manuscript online 11 November 2024)

Electromagnetic wave-absorbing materials play a crucial role in modern electronics, particularly in stealth and communication technologies. Carbon-based materials demonstrate considerable potential for the development and use of effective wave-absorbing substances, attributed to their complex structure, lightweight nature, excellent corrosion resistance, and affordability. Notably, nitrogen-doped carbon-based two-dimensional (2D) materials exhibit a more pronounced depletion effect on electromagnetic waves owing to their increased specific surface area and numerous polarization states. This article presents the successful synthesis of nitrogen-doped carbon (NC) 2D flakes using a hydrothermal method. In addition, single Fe atoms were successfully incorporated onto their surfaces, forming Fe@NC. The wave-absorbing capabilities of the Fe@NC samples were considerably improved, achieving a minimum reflection loss (RLmin) of −69.22 dB at 11.48 GHz and an effective absorption bandwidth of 5.79 GHz. The enhancement in electromagnetic wave absorption is attributed to the synergistic effects of magnetic loss, relaxation processes, dipole polarization, and electrical conduction loss. The successful synthesis of Fe@NC opens up new avenues for the development of atomically dispersed wave-absorbing materials.

DOI: 10.1088/0256-307X/41/12/128401

1. Introduction. Wave-absorbing materials serve as mediums that effectively absorb electromagnetic waves and minimize their reflection, making them essential in various modern technology sectors, including military and communications.[1–3] Notably, they are extensively used in stealth technology, enabling aircraft, ships, and other military equipment to decrease the likelihood of radar detection.[4,5] Furthermore, in communication, these materials help mitigate electromagnetic interference, ensuring stable transmission of communication signals. With the ongoing advancement of science and technology, the demand for wave-absorbing materials is increasing. Carbon-based materials, known for their lightweight nature, high absorption strength, and broad absorptive bandwidth, have emerged as a hotspot for research.[6,7] These materials not only fulfill the need for lightweight solutions but also demonstrate effective absorption of electromagnetic waves over a wider frequency range.[8,9]

In recent years, nitrogen-doped carbon (NC) two-dimensional (2D) materials have demonstrated considerable potential for wave-absorption applications, attributed to their distinctive microstructures and ultralight characteristics.[10–12] These materials possess a high specific surface area and a rich pore structure, which enhance the absorption and dissipation of electromagnetic waves. Moreover, their properties can be further fine-tuned through the incorporation of nitrogen atoms. For instance, Yan *et al.* successfully prepared nitrogen-doped graphene-like carbon nanonets (N–GNs) by thermally exfoliating two-dimensional MOFs using KCl and LiCl.[13] This material achieved a minimum reflection loss (RL_{min}) of −54 dB at a thickness of 2.1 mm and a filler addition of 3 wt%. This enhancement in performance can be attributed to improved impedance matching resulting from the micro–medium–macroporous structure, dipole polarization arising from nitrogen heteroatoms and surface defects, and interfacial polarization, as well as conductivity loss owing to the abundance of heterogeneous graphene interfaces. Similarly, Wang *et al.* developed two-dimensional N/O carbon nanowires (N–GNs) through the straightforward carbonization of a polyurea (PU) nanosheet made from p-phenylene diisocyanate (PDIC) and urea, leading to the formation of two-dimensional N/O codoped carbon nanonets (NOCN). These samples demonstrated optimal microwave absorption properties at a carbonization temperature of 900 ℃ (NOCN-900), with an RL_{min} value of −54.2 dB, an effective absorption bandwidth (EAB) of 7.44 GHz, and a thickness of 2.3 mm at a filler content

†These authors contributed equally to this work.
*Corresponding author. Email: wuyf128@bupt.edu.cn; pxchxc@njust.edu.cn
© 2024 Chinese Physical Society and IOP Publishing Ltd

of just 5 wt%. This preparation process facilitates easy control over the degree of graphitization, porous structure, sheet size, and heteroatom doping content by adjusting the carbonization temperature. However, single nitrogen-doped carbon materials still fall short in terms of their wave-absorbing strength. Consequently, researchers have begun investigating the incorporation of magnetic loss mechanisms by adding magnetic particles such as iron, cobalt, and nickel to further improve the wave-absorbing properties of these materials.[14–16] Drawing inspiration from the geomorphology of sea cucumbers, Yan *et al.* developed Nb_2CT_x@Co nitrogen-doped carbon nanosheet arrays@carbon fiber aerogels through self-assembly, *in situ* chemical deposition, and subsequent pyrolysis, resulting in Nb_2CT_x@Co–NC@CFA.[17] The presence of numerous heterogeneous interfaces between Nb_2CT_x and Co nitrogen-doped carbon nanosheet arrays considerably enhanced the electromagnetic wave polarization loss and optimized impedance matching. This material achieved an EAB of 2.96 GHz (8.48–11.44 GHz) at a thickness of 2.36 mm and 5.2 GHz (12.8–18 GHz) at 1.6 mm. Despite these advancements, research on the loading of magnetic nanoparticles onto NC nanosheet substrates for wave-absorbing materials remains scarce, and this approach has yet to be thoroughly investigated.

Single-atom materials have emerged as a research hotspot in recent years, attracting intensive study and widespread application in the field of electrocatalysis.[18–20] Metal monoatomic-loaded nitrogen-doped carbon materials have generated considerable research interest as electromagnetic wave-absorbing materials owing to the strong metal-carrier interactions and extremely high surface energies exhibited by the isolated metal atoms.[21,22] The differing electronegativities between the isolated metal atoms and the adjacent nonmetal atoms enable the transfer of electrons from the metal monoatoms to the nonmetal atoms, facilitating the modulation of the electronic properties of carbon.[23] On the one hand, this charge redistribution enhances the electrical conductivity of the host nanocarbon, leading to an increase in conduction loss.[24] On the other hand, metal atoms can act as polarization centers that oscillate in response to an external electromagnetic field, thereby enhancing relaxation loss.[25] Hu *et al.* introduced a novel method for synthesizing Co single-atom and Co cluster-level electromagnetic wave absorbers with controllable dipole moments, establishing a relationship between polarization loss and electromagnetic wave absorption on an atomic scale.[26] By adjusting the concentration of Co atoms, they successfully modulated the valence state of the Co atoms between 0 and +2, enabling control over dipole polarization and relaxation. The findings indicate that a Co concentration of 6.0 wt% achieves an optimal dipole moment, leading to exceptional absorption performance with an RL_{min} exceeding −54.3 dB and an EAB of 7.0 GHz at a thickness of 2.0 mm. Shi *et al.* introduced a dicyandiamide-mediated pyrolysis strategy to partially anchor five nitrogen-coordinated lanthanum (La)–N_5 to N-doped graphene nanocages.[27] The resulting composite, along with aramid nanofibers forming a polydimethylsiloxane-coated chemically crosslinked film, demonstrated remarkable electromagnetic wave-absorption capabilities, achieving an EAB of 6.24 GHz at a thickness of 2.0 mm. Therefore, single atoms can be further explored and validated in the development and application of wave-absorbing materials.

In this study, we successfully incorporated Fe single atoms onto nitrogen-doped carbon two-dimensional nanosheets (NC), following this design concept, resulting in a substantial improvement in the wave-absorption properties of the materials. Notably, the Fe@NC sample demonstrated outstanding performance in wave absorption, attributed to enhanced magnetic loss and relaxation processes, along with considerable dipole polarization and conduction loss. This resulted in a considerable decrease in RL_{min} to −67.23 dB and an expansion of the EAB to 5.22 GHz. These findings not only confirm the viability of this design concept but also present a new opportunity for the advancement of atomically dispersed wave-absorbing materials. Additionally, they yield fresh insights into the development of materials aimed at enhancing efficient electromagnetic response functions. Moving forward, Fe@NC materials are expected to contribute considerably to these areas and support the continued advancement and application of related technologies.

2. Experimental Sections.

2.1. Materials. Urea ($CO(NH_2)_2$, 99%, Aladdin), citric acid ($C_6H_8O_7$, 99.5%, Aladdin), and iron(III) nitrate nonahydrate ($Fe(NO_3)_3{\cdot}9H_2O$, 99.9%, Aladdin) were used as received without any further purification in this work.

2.2. Preparation of the NC and Fe@NC. Urea and citric acid were used as the nitrogen and carbon sources, respectively, each in a quantity of 6 g. All precursors were combined in 40 ml of deionized water and gently stirred for 1 h. The resulting mixture was then transferred to a stainless steel Teflon-sealed hydrothermal reactor and subjected to heat treatment at 160 ℃ for 6 h to yield a dark green colloidal solution. After this, the solution was centrifuged at 12000 rpm to eliminate larger particles and thoroughly rinsed multiple times with ethanol to remove any unreacted precursors. Subsequently, the powder samples were subjected to additional heat treatment and annealing at 800 ℃ for 3 h in an Ar atmosphere, with a ramp rate of 2 ℃/min, and maintained for 2 h to produce nitrogen-doped NC. The synthesis process for the N-doped carbon 2D nanosheets incorporating Fe single atoms closely mirrors that of the NC, with the exception that during the initial step, an additional 0.1 g of $Fe(NO_3)_3{\cdot}9H_2O$ is introduced into the mixed solution.

Permittivity and permeability tests were performed by mixing various concentrations of NC or Fe@NC with paraffin wax. Initially, a specified amount of paraffin wax was thoroughly dissolved in ether, after which NC or Fe@NC was added, followed by stirring and sonication to achieve a uniform mixture. The concentrations used in the study were 5, 10, 15, and 20 wt%. All samples not explicitly stated in the article defaulted to a concentration of 15 wt%.

Finally, the ether was entirely evaporated through sonication and heating, and the resulting solid was molded into the required shape for the coaxial testing method.

2.3. Materials Characterization. X-ray powder diffraction data were obtained using an XRD (D/max 2500, Rigaku, Japan) using Cu Kα radiation (λ = 1.54178 Å). Micromorphological images were captured using a field emission scanning electron microscope (FE-SEM, LEO-1530, Zeiss, Germany) equipped with an energy dispersive spectrometer (EDS) attachment. TEM analysis was performed on a 2100F transmission electron microscope operating at 200 kV, as well as an aberration-corrected transmission electron microscope (JEM-ARM200F) also functioning at an accelerating voltage of 200 kV. Surface element information was gathered using an X-ray photoelectron spectrometer (ESFalab 250Xi, Thermo Fisher, America), which included an Al Kα radiation source (1487.6 eV) and a hemispherical analyzer set to a pass energy of 30 eV. Thermogravimetric analysis (TGA) was performed using a thermogravimetric analyzer (STA 449 F3, Jupiter, Germany). The surface temperature of the samples was monitored with an infrared (IR) thermal imager (CEM DT-980, Huashengchang, China). Raman spectra were acquired using a laser Raman spectrometer (HR Evolution, HORIBA). The magnetic properties were assessed using a high-sensitivity magnetic measurement system (SQUID-VSM (MPMS-3), Quantum Design).

2.4. Measurement and Calculation of the Electromagnetic Properties. The real (ε') and imaginary (ε'') parts of permittivity, as well as the real (μ') and imaginary (μ'') parts of permeability, were directly measured using a vector network analyzer (N5224B, Keysight). For the coaxial method, the absorbers were shaped as required for measurement, with an outer radius of 7 mm and an inner radius of 3 mm. The equations for RL_{min}, the attenuation constant (α), and impedance matching (Z_{in}/Z_0) are provided in the supporting information. [20,28–30]

3. Results and Discussion. Nitrogen-doped NC and Fe single-atom loaded nitrogen-doped carbon 2D nanosheets (Fe@NC) were successfully synthesized following the established method. [31] A schematic illustration of the preparation process is presented in Fig. 1. The XRD spectra revealed peaks at 25.3° and 44.2°, which correspond to the two crystal planes (002) and (101) of carbon [Fig. 2(a)]. [32] Notably, the XRD spectrum did not show any peaks for Fe, indicating that it was present in a monoatomic form. Thermogravimetric analysis was performed in an air environment [Figs. 2(b) and 2(c)]. Figure 2(b) shows that NC completely lost its mass after full combustion. Meanwhile, 6.6 wt% of Fe@NC remained, indicating that Fe was likely in the form of Fe_3O_4. Consequently, the initial loading of the Fe single atoms was estimated to be 4.78 wt%. The Raman spectrum revealed a slight Fe peak at 600 cm^{-1}, along with the D and G peaks associated with carbon at 1347 and 1579 cm^{-1}, respectively [Fig. 2(d)]. [33] In the fourier transform infrared spectrometer (FTIR) spectra, both samples displayed characteristic peaks at 880, 1042, 1540, 2900, and 3390 cm^{-1}, corresponding to the bending and stretching vibrations of C–H, C–O, C–C, C–H, and –OH, respectively [Fig. 2(e)]. [34] In contrast, Fe@NC showed a C–N characteristic peak at 1090 cm^{-1}. The SQUID curves confirmed that the successful incorporation of Fe single atoms induced ferromagnetism in Fe@NC [Fig. 2(f)]. The Fe@NC sample exhibited a critical magnetic field strength (H_c) of 30.6 Oe and a saturation magnetization strength (M_s) of 3.7×10^{-4} emu/g. Additional experiments confirmed the successful doping of nitrogen and the incorporation of Fe, as reflected in the XPS results. However, the Fe 2*p* peak was not distinctly visible in the XPS survey owing to the low Fe content compared to C (Fig. S1 in Supplementary Information). In the XPS C 1*s* maps for both samples, a peak corresponding to C–N was detected at 286.2 eV [Fig. 2(g) and Fig. S2(a)]. In the XPS N 1*s* mapping, the Fe@NC sample displayed a distinct peak for Fe–N_x at 399.2 eV [Fig. 2(h)]. [35] The other peaks observed at 398.1, 400.1, 400.7, and 403.3 eV were attributed to pyridinic N, pyrrolic N, graphitic N, and oxidized N, respectively, which corresponded to the NC sample [Fig. S2(b)]. The XPS Fe 2*p* spectrum of the Fe@NC sample showed clear peaks at 709.9 and 723.1 eV, indicating the $2p_{3/2}$ and $2p_{1/2}$ states of Fe (II) [Fig. 2(i)]. The valence state of Fe was affected by the high electronegativity of nitrogen. Characteristic signals of Fe were not present in the XPS Fe 2*p* spectrum of the NC sample [Fig. S2(c)].

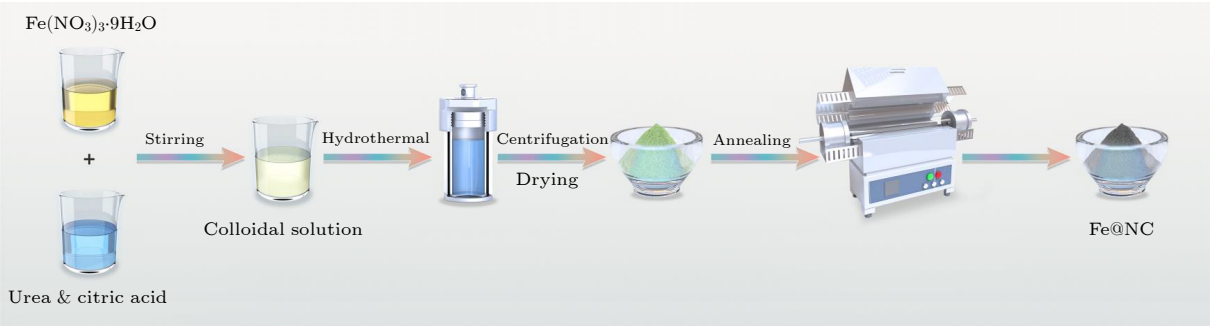

Fig. 1. Schematic representation of the preparation process for NC and Fe@NC.

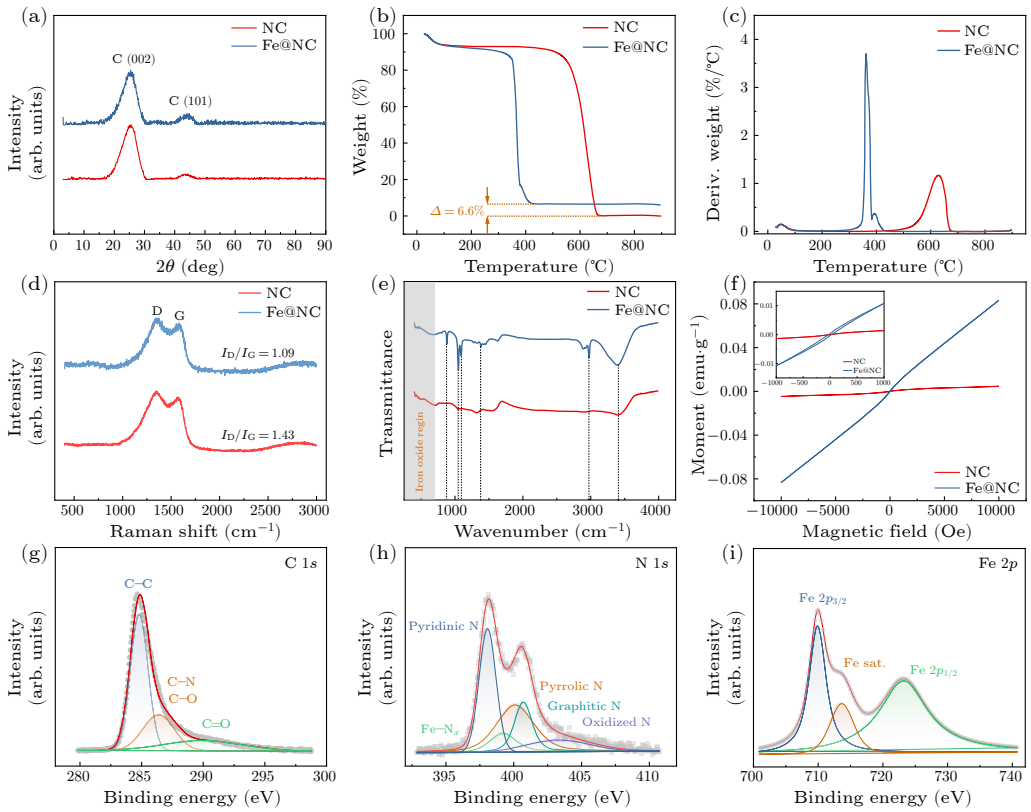

Fig. 2. Structural characterizations of the NC and Fe@NC samples. (a) XRD patterns, (b) TGA curve, (c) Derivative thermogravimetry curve, (d) Raman spectra, (e) FTIR spectrum, (f) SQUID curves, (g) XPS C 1*s* spectrum of Fe@NC, (h) XPS N 1*s* spectrum of Fe@NC, and (i) XPS Fe 2*p* spectrum of Fe@NC.

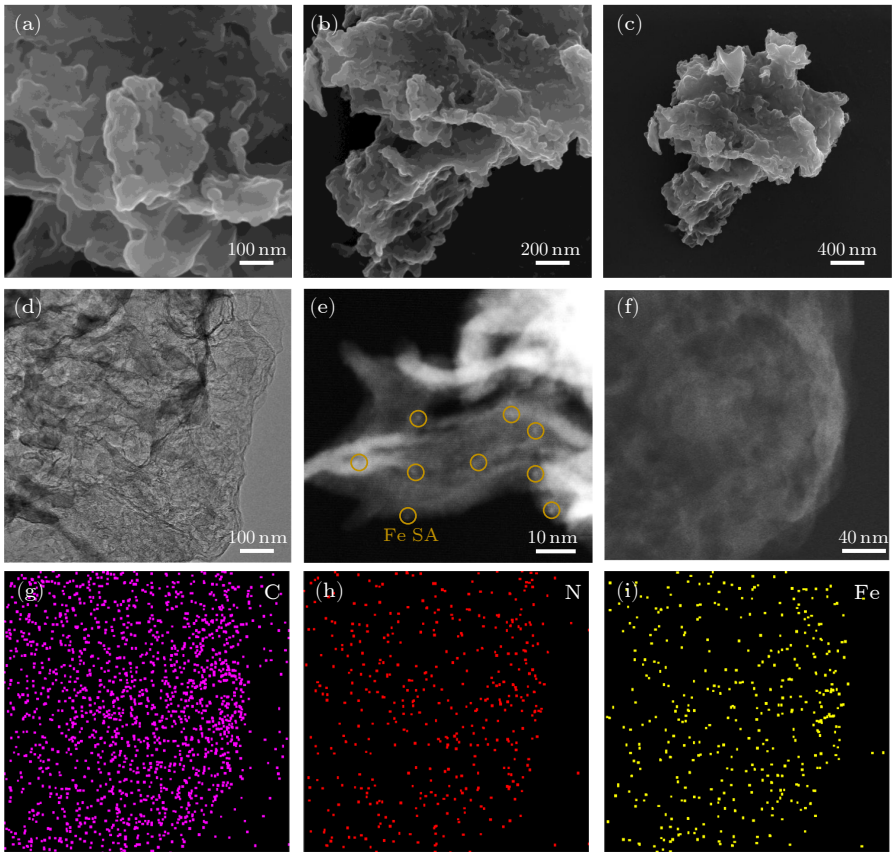

Fig. 3. Morphological characterizations of the NC and Fe@NC samples. (a)–(c) SEM images of Fe@NC. (d, e) TEM images of Fe@NC. (f)–(i) TEM–EDS of Fe@NC.

The micro-morphology of the NC and Fe@NC samples was analyzed using SEM, revealing that both exhibited two-dimensional, sheet-like stacked structures [Figs. 3(a)–3(c) and Fig. S3]. Notably, the smallest unit 2D sheet of Fe@NC measured approximately 100 nm, which formed micrometer-sized agglomerates upon stacking. TEM analysis confirmed the presence of both the thinner 2D sheet structure of Fe@NC and its stacked configuration, corresponding to the light and dark regions in Fig. 3(d), respectively. Similar structures were also noted in Fig. S4. The difference was that, in the Fe@NC sample, the NC surface exhibited visible Fe monoatomic particles at higher magnification, as indicated in the labeled section of Fig. 3(e).[36] The TEM–EDS analysis of this sample clearly demonstrated a uniform distribution of the elements C, N, and Fe. Likewise, C and N were also found to be uniformly distributed in the NC sample (Fig. S5).

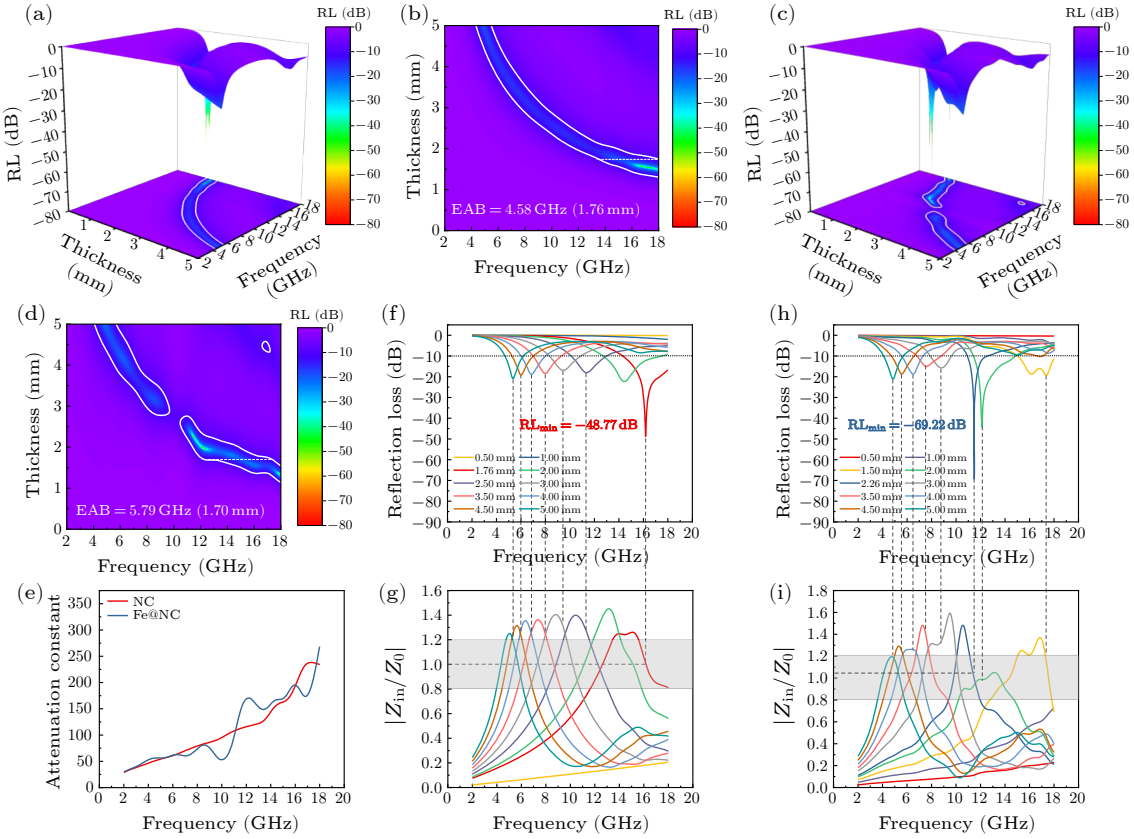

Fig. 4. Electromagnetic wave-absorption characteristics of the NC and Fe@NC samples. (a) Three-dimensional representation of the reflection loss of NC. (b) Two-dimensional representation of the reflection loss of NC. (c) Three-dimensional representation of the reflection loss of Fe@NC. (d) Two-dimensional representation of the reflection loss of Fe@NC. (e) Attenuation constants for NC and Fe@NC. (f) RL across different thicknesses of NC. (g) Impedance matching for the NC sample at various thicknesses. (h) RL across different thicknesses of Fe@NC. (i) Impedance matching for the Fe@NC sample at various thicknesses.

The wave-absorption properties of the 5, 10, 15, and 20 wt% samples containing NC and Fe@NC were evaluated in the 2–18 GHz frequency range. Among these, both 15 wt% samples demonstrated excellent wave-absorption capabilities. Figure 4(a) shows the wave-absorption performance of the NC 15 wt% sample, which achieved an RL_{min} of −48.77 dB at 1.76 mm and 16.18 GHz [Fig. 4(b)]. This sample also exhibited the broadest wave-absorption bandwidth for its thickness, with an EAB of 4.58 GHz [Fig. 4(b)]. In comparison, the NC 5 wt% samples, also presenting an EAB of 4.58 GHz [Fig. 4(b)], exhibited a comparable RL_{min} of −48.77 dB. However, the NC 5 wt% and NC 10 wt% samples demonstrated inadequate wave-absorption capabilities in the 2–18 GHz range [Figs. S6(a)–S6(d)]. In contrast, the NC 20 wt% samples exhibited strong wave-absorption performance at specific thicknesses, particularly in the frequency ranges of 8.6–10.2 GHz and 15.1–18.0 GHz [Figs. S6(d) and S6(e)]. The addition of a single Fe atom considerably improved the absorption performance of the Fe@NC samples compared to the NC samples. Figures 4(c) and 4(d) show the absorption performance of the Fe@NC 15 wt% samples, which achieved an RL_{min} of −69.22 dB at 2.26 mm and 11.48 GHz. The broadest absorption bandwidth was recorded at a thickness of 1.70 mm, yielding an EAB of 5.79 GHz [Fig. 4(d)]. The Fe@NC samples exhibited no wave absorption at the 5 wt% fill rate, while the absorption bandwidths at 10 and 20 wt% fill rates were notably shorter, measuring 0.5 and 2.21 GHz, respectively (Fig. S7). The attenuation constants α for both the NC

and Fe@NC samples increased with frequency across the 2–18 GHz range. Overall, the α value for the Fe@NC sample was found to be equivalent to that of the NC sample [Fig. 4(e)]. Figure 4(f) shows the RL and absorption bandwidths of the NC 15 wt% sample at different thicknesses, revealing that the effective absorption bandwidth shifted to lower frequencies as thickness increased. The RL_{min} indicated a favorable impedance match with $|Z_{in}/Z_0| = 1$ [Fig. 4(g)]. Similarly, Fig. 4(h) shows that the EAB of the Fe@NC 15% sample also shifted to lower frequencies with increased thickness, with the RL_{min} indicating a good impedance match of $|Z_{in}/Z_0| = 1.05$ [Fig. 4(i)]. The incorporation of Fe single atoms considerably improved both the wave-absorbing strength and effective wave-absorbing bandwidth of NC. Thus, Fe@NC can be regarded as an exceptional wave-absorbing material.

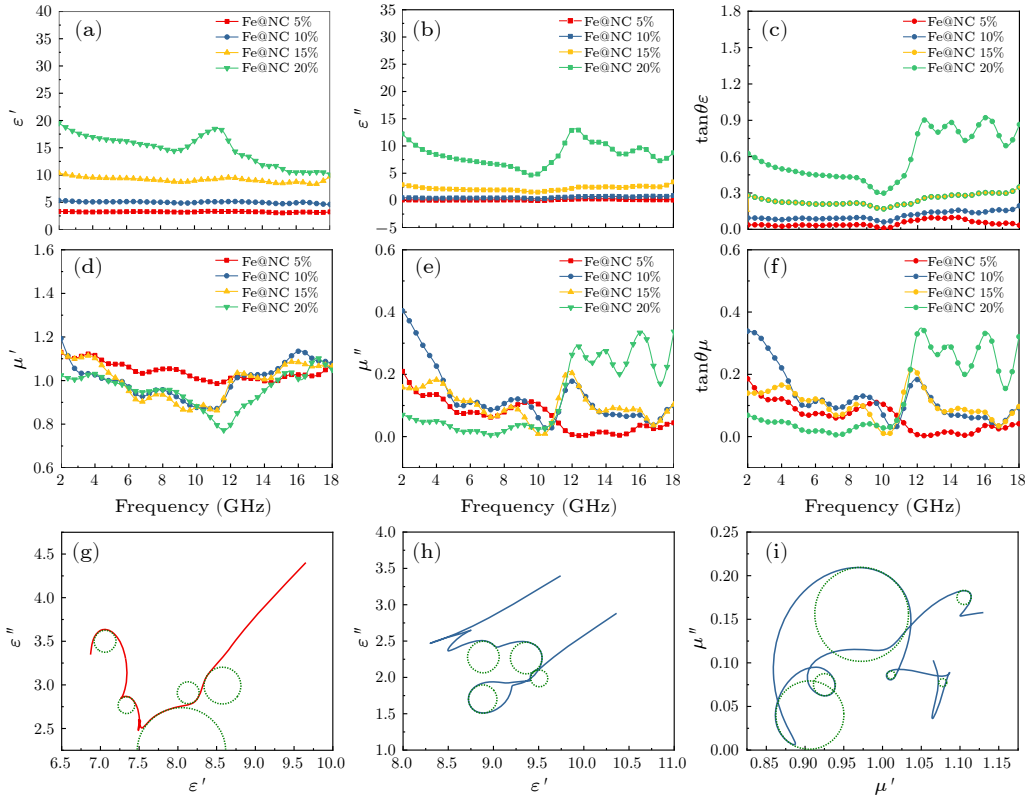

Fig. 5. Electromagnetic characteristics of the NC and Fe@NC samples. (a) Real part of permittivity ε' for mixtures of paraffin and Fe@NC with varying contents. (b) Imaginary part of permittivity ε'' for mixtures of paraffin and Fe@NC with varying contents. (c) Dielectric loss angle tangent $\tan\theta_\varepsilon$ for mixtures of paraffin and Fe@NC with varying contents. (d) Real part of permeability μ' for mixtures of paraffin and Fe@NC with varying contents. (e) Imaginary part of permeability μ'' for mixtures of paraffin and Fe@NC with varying contents. (f) Magnetic loss angle tangent $\tan\theta_\mu$ for mixtures of paraffin and Fe@NC with varying contents. (g) Dielectric Cole–Cole curve for NC. (h) Dielectric Cole–Cole curve for Fe@NC. (i) Magnetic Cole–Cole curve for Fe@NC.

The positive effect of Fe single-atom loading on improving the wave-absorption performance of NC was evaluated through the dielectric constant and permeability. For both NC and Fe@NC, the real and imaginary components of the dielectric constant, as well as the tangent of the loss angle, increased with the amount of filling [Figs. 5(a)–5(c) and Figs. S8(a)–S8(c)]. In contrast, the real part of the permittivity for Fe@NC was comparable to that of NC at similar filling amounts, while its imaginary part and the tangent of the dielectric loss angle were lower than those of NC. This variation is attributed to the effective incorporation of the Fe single atoms. Fe@NC demonstrated substantially improved permeability and magnetic loss [Figs. 5(d)–5(f)]. Figure 5(g) shows the Cole–Cole curves of the NC samples, as defined in Eq. 3. Based on the ideal Debye relaxation model, the ε'–ε'' curve should appear as a semicircle, with each circle representing a relaxation polarization process. This sample exhibited a rich relaxation polarization in the electromagnetic field, attributed to the extensive surface area of its two-dimensional lamellar structure. Additionally, Fe@NC displayed a relaxation polarization process similar to that of NC [Fig. 5(h)]. The straight line at the end of the Cole–Cole curve indicated the presence of conduction loss; thus, both samples experienced considerable conduction loss owing to the excellent electrical conductivity of the carbon-based material. Similar to the Cole–Cole curve of permittivity, the magnetic permeability Cole–Cole curve also reflected the resonant loss process.[37] Therefore, the incorporation of Fe single atoms imparted multiple magnetic resonance loss processes to the Fe@NC samples [Fig. 5(i)]. It is widely acknowledged that magnetic losses in the 2–18 GHz range primarily arise from natural resonances, eddy current losses, and exchange resonances. The eddy current loss can be repre-

sented by C_0 (Eq. 6). Figure S9 shows the C_0 value of the Fe@NC sample, which varies with frequency, suggesting that eddy current loss is not the primary contributor to magnetic loss. However, a distinct peak representing eddy current loss is evident at 10 GHz. Moreover, the curve exhibits peaks around 6 GHz owing to the natural resonance of the magnetic particles, while the exchange resonance peaks near 15 GHz arise from Fe single atoms.[38,39] Overall, the Fe@NC samples experienced a notable enhancement in magnetic loss, alongside a slight increase in relaxation loss, and the inherent high conduction loss of the NC substrate, resulting in a considerably improved RL.[40–42] The related electromagnetic wave-absorption mechanism is shown in its entirety in Fig. 6.

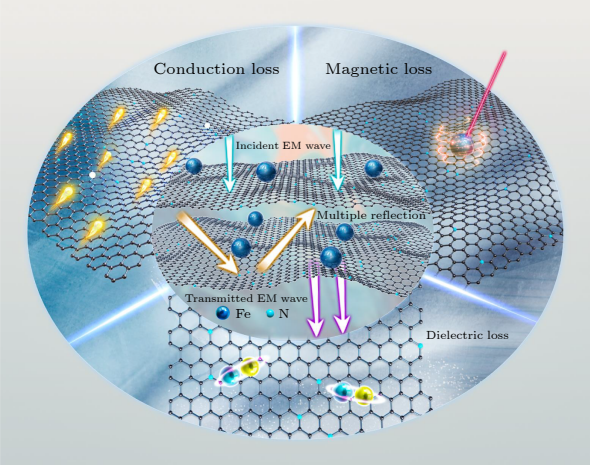

Fig. 6. Schematic diagram of the electromagnetic wave-absorption mechanism.

4. Conclusion. In this study, Fe was effectively incorporated into nitrogen-doped NC, resulting in the preparation of Fe@NC samples. These Fe@NC samples demonstrated a considerable enhancement in wave-absorption performance compared to NC. Notably, Fe@NC achieved an outstanding RL_{min} of −69.22 dB at 11.48 GHz with a thickness of 1.93 mm, exceeding the RL_{min} of −48.77 dB for NC at 16.18 GHz with a thickness of 1.76 mm. Additionally, the EAB of Fe@NC increased to 5.79 GHz, compared to 4.58 GHz for NC. These enhancements were ascribed to the improved magnetic loss and relaxation processes stemming from the presence of Fe single atoms, which also contributed to enhanced permeability and impedance matching. Coupled with the abundant dipole polarization inherent to the NC sample owing to N atoms and surface defects, along with the excellent conductivity losses associated with the carbon-based material, Fe@NC exhibited strong electromagnetic absorption capabilities. The benefits of Fe@NC include its lightweight nature, strong absorption efficiency, and wide bandwidth, making it a promising candidate for advanced electromagnetic interference shielding and stealth technology.

Acknowledgements. This work was supported by the Fundamental Research Funds for the Central Universities (Grant No. 2021XD-A04-2), the National Natural Science Foundation of China (Grant Nos. 61874014 and 61874013), the Fund of State Key Laboratory of Information Photonics and Optical Communications (Beijing University of Posts and Telecommunications, China), and BUPT Excellent Ph. D. Students Foundation (Grant No. CX2022237).

References

[1] Wu C, Chen Z, Wang M, Cao X, Zhang Y, Song P, Zhang T, Ye X, Yang Y, Gu W, Zhou J, and Huang Y 2020 *Small* **16** 2001686
[2] Xia Y, Gao W, and Gao C 2022 *Adv. Funct. Mater.* **32** 2204591
[3] Lou Z, Wang Q, Kara U I, Mamtani R S, Zhou X, Bian H, Yang Z, Li Y, Lv H, Adera S, and Wang X 2021 *Nano-micro Lett.* **14** 11
[4] Sun X, Li Y, Huang Y, Cheng Y, Wang S, and Yin W 2022 *Adv. Funct. Mater.* **32** 2107508
[5] An Q, Li D, Liao W, Liu T, Joralmon D, Li X, and Zhao J 2023 *Adv. Mater.* **35** 2300659
[6] Fang Y, Wang W, Wang S, Xue W, and Zhao R 2023 *J. Phys.: Conf. Ser.* **2437** 012053
[7] Zhang Z, Zhao Y, Li Z, Zhang L, Liu Z, Long Z, Li Y, Liu Y, Fan R, Sun K, and Zhang Z 2022 *Adv. Compos. Hybrid Mater.* **5** 513
[8] Hou S, Wang Y, Gao F, Yang H, Jin F, Ren L, Wu Q, Ge H, and Wang Y 2023 *Chem. Eng. J.* **471** 144779
[9] Kong L, Zhang S, Liu Y, Wu H, Fan X, Cao Y, and Huang J 2023 *Carbon* **207** 198
[10] Inagaki M, Toyoda M, Soneda Y, and Morishita T 2018 *Carbon* **132** 104
[11] Hu X, Long Y, Fan M, Yuan M, Zhao H, Ma J, and Dong Z 2019 *Appl. Catal. B-Environ.* **244** 25
[12] Zhou J, Jiang L, Shu C, Kong L, Ahmad I, Zhou Y N, Tang W, Sun X, and Wu Y 2021 *Energy Environ. Mater.* **4** 569
[13] Yan J, Wang Y, Liu W, Liu P, and Chen W 2023 *J. Colloid Interface Sci.* **643** 318
[14] Dedi, Idayanti N, Kristiantoro T, Sudrajat N, Gustinova A, and Primadona I 2019 *IOP Conf. Ser.: Mater. Sci. Eng.* **553** 012001
[15] Liu T, Zhang Y, Wang C, Kang Y, Wang M, Wu F, and Huang W 2024 *Small* **20** 2308378
[16] Sun M, Xiong Z, Zhang Z, Chen C, Qin L, Wang D, Wu F, and Liu P 2022 *Compos. Sci. Technol.* **228** 109663
[17] Yan J, Cui C, Bai W, Tang H, and Guo R 2024 *Nano Research* **17** 9261
[18] Gawande M B, Fornasiero P, and Zbořil R 2020 *ACS Catalysis* **10** 2231
[19] Xiong H, Datye A K, and Wang Y 2021 *Adv. Mater.* **33** 2004319
[20] Guo W, Wang Z, Wang X, and Wu Y 2021 *Adv. Mater.* **33** 2004287
[21] Zhang X, Li B, Xu J, Zhang X, Shi Y, Zhu C, Zhang X, and Chen Y 2023 *Adv. Funct. Mater.* **33** 2210456
[22] Cao K, Xue W, and Zhao R 2024 *J. Phys.: Conf. Ser.* **2706** 012029
[23] Deng D, Chen X, Yu L, Wu X, Liu Q, Liu Y, Yang H, Tian H, Hu Y, Du P, Si R, Wang J, Cui X, Li H, Xiao J, Xu T, Deng J, Yang F, Duchesne P N, Zhang P, Zhou J, Sun L, Li J, Pan X, and Bao X 2015 *Sci. Adv.* **1** e1500462
[24] Bayatsarmadi B, Zheng Y, Vasileff A, and Qiao S Z 2017 *Small* **13** 1700191
[25] Zhang X, Guo J, Guan P, Qin G, and Pennycook S J 2015 *Phys. Rev. Lett.* **115** 147601
[26] Liu H, Li X, Zhao X, Zhang M, Liu X, Yang S, Wu H, and Ma Z 2023 *Adv. Funct. Mater.* **33** 2304442
[27] Shi Y, Ma Z, Zhang X, Ma Z, Yan F, Zhu C, and Chen Y 2024 *Adv. Funct. Mater.* **34** 2403508
[28] Yao J, Zhou J, Yang F, Peng G, Liu Y, Yao Z, Wu F, and Zeng H 2024 *Nano Research* **17** 3359

[29] Han M, Yang Y, Liu W, Zeng Z, and Liu J 2022 *Sci. China Mater.* **65** 2911
[30] Wang J, Liu L, Jiao S, Ma K, Lv J, and Yang J 2020 *Adv. Funct. Mater.* **30** 2002595
[31] Agour A M, Elkersh E, Khedr G E, El-Aqapa H G, and Allam N K 2023 *ACS Appl. Nano Mater.* **6** 15980
[32] Zhao Y, Nakamura R, Kamiya K, Nakanishi S, and Hashimoto K 2013 *Nat. Commun.* **4** 2390
[33] Narimisa S, Mouradzadegun A, Zargar B, and Ganjali M R 2024 *Inorg. Chem. Commun.* **167** 112793
[34] Wu X, Wang Z, Chen K, Li Z, Hu B, Wang L, and Wu M 2021 *ACS Appl. Mater. Interfaces* **13** 22448
[35] Jiao L, Wan G, Zhang R, Zhou H, Yu S H, and Jiang H L 2018 *Angew. Chem. Int. Edit.* **57** 8525
[36] Jiao L, Zhang R, Wan G, Yang W, Wan X, Zhou H, Shui J, Yu S H, and Jiang H L 2020 *Nat. Commun.* **11** 2831
[37] Wu Y, Li Q, Li Y, Li C, Zhou Y, Du P, Cao W, He X, Liu Z, Xu J, Huang K, Lei M, Bi K, and Wu H 2024 *Carbon* **229** 119474
[38] Lv S, Luo H, Wang Z, Yu J, Cheng Y, Chen F, and Li X 2024 *Carbon* **218** 118668
[39] Chen F, Zhang S, Ma B, Xiong Y, Luo H, Cheng Y, Li X, Wang X, and Gong R 2022 *Chem. Eng. J.* **431** 134007
[40] Zeng Y, Almatrafi E, Xia W, Song B, Xiong W, Cheng M, Wang Z, Liang Y, Zeng G, and Zhou C 2023 *Coord. Chem. Rev.* **475** 214874
[41] Xie F, Wang C, Li Y, and Yao Y 2023 *ACS Appl. Electron. Mater.* **5** 6037
[42] Fu Z, Wu Y, Li Y, Huang K, Li Q, Yao H, Cao W, Gao S, Qin Y, Zheng Z, Xu J, Lei M, Bi K, and Wu H 2024 *J. Materiomics* 100936